Mem. S.A.It. Vol. 92, 11

Memorie della

Development of the polarization modulator and multi-mode receivers for the search of CMB polarization

F. Columbro[1,2]

[1] Dipartimento di Fisica, Sapienza Università di Roma, P.le A. Moro 5, 00185, Roma, Italy
[2] INFN–Sezione di Roma1, P.le A. Moro 5, 00185, Roma, Italy e-mail: fabio.columbro@roma1.infn.it

Abstract. The most ambitious challenge in Experimental Cosmology today is the accurate measurement of the polarized signal of the Cosmic Microwave Background (CMB). This paper is focused on two of the critical instrumental challenges in the polarization measurement which forthcoming experiments like LSPE/SWIPE and LiteBIRD will deal with: the receivers and the polarization modulation system. SWIPE is one of the two instruments of the Large Scale Polarization Explorer (LSPE) which aims to measure the CMB polarization at large angular scale with a goal of tensor to scalar ratio $r = 0.01$. The detection of this tiny signal requires a very large array of polarization-sensitive detectors coupled to an imaging optical system to obtain a wide field of view. The development and testing status of a multi-mode pixel assembly is presented.
In the second part of the paper we present the status of the polarization modulator. This system offers a solution to disentangle the polarized signal of interest from these unpolarized foregrounds and a rapidly-rotating half-wave plate is the most promising scheme. The LSPE/SWIPE polarization modulator unit operates at 1.6 K and is based on magnetic levitation which can significantly reduce the friction. A large number of tests were performed on a room temperature mockup and the optimized configuration is presented. A polarization modulator similar to the LSPE/SWIPE one will be used in the LiteBIRD mission, the next generation satellite mission planned to be operative in $\sim$ 10 years, which will map CMB polarization 20 times deeper than Planck, with a total error of $\delta r < 0.001$. The development of the two polarization modulator units is more challenging than for SWIPE due to the spacecraft requirements and the Technology Readiness Level (TRL) required.

1. Introduction

The search for the primordial B-modes in the polarization of the Cosmic Microwave Background (CMB) is the main challenge in the experimental cosmology. After its discovery Penzias and Wilson 1965 the CMB represents an essential source of information about all epochs of the universe. The cold dark matter model (ΛCDM) gives us the most accurate description of the constituents and the evolution of the universe and can be extended by adding cosmological inflation, a short period of exponential expansion in the very early universe. Inflation's basic predictions Guth 1981 regarding the universe large-scale geometry and structure have been borne out by cosmo-

logical measurements to date. Inflation predicts also the existence of a background of gravitational waves, or tensor mode perturbations. The amplitude of tensors is conventionally parameterized by r, the tensor-to-scalar ratio at a fiducial scale, and its imprint in the CMB polarization is a direct measure of the energy scale of inflation. Theoretical predictions of the value of r cover a very wide range. Conversely, a measurement of r can discriminate between models of inflation. The current upper limit is $r < 0.06$ at 95% confidence Planck Collaboration 2020.

The detection of this tiny signal requires a very large array of polarization-sensitive detectors coupled to an imaging optical system to obtain a wide field of view, thus maximizing the mapping speed. Current and forthcoming experiments are designed with this philosophy (thousands of detectors and a modulation technique), but each approach is quite different from the other depending on the location and the strategy Thornton et al. 2016, Grayson et al. 2016, Polarbear Collaboration 2020, Mennella et al. 2019, Battistelli et al. 2020, Gualtieri et al. 2018, Benson et al. 2014.

Another promising instrument is SWIPE de Bernardis et al. 2012, one of the two instruments of the Large-Scale Polarization Explorer (LSPE) experiment Aiola et al. 2012, Lamagna et al. 2020, LSPE Collaboration 2021 which aims to measure the polarization of the CMB at large angular scale with a goal of $r = 0.01$. SWIPE is the balloon-borne instrument which will be launched from Longyearbyen during the arctic night. After other experiments launched during the summer Masi et al. 2019, Paiella et al. 2019, SWIPE will be the first scientific long duration balloon launched from the arctic pole during the winter. SWIPE will focus the incoming radiation on two large curved focal planes (at a temperature of 0.3 K) hosting 326 multi-mode pixels with Transition Edge Sensor (TES) thermistors, divided in the 3 frequency bands: 145 GHz (30% bandwidth), 210 GHz (20% bandwidth) and 240 GHz (10% bandwidth). A 145 GHz sample was tested in a customized 0.3 K cryostat, using also a cryogenic neoprene absorber, developed to reduce the background on the detector at a level similar to the one expected in flight, allowing to measure the main beam of the pixel assembly (see §2).

Unfortunately the CMB polarization signal is well below the level of unpolarized foregrounds. This makes systematic errors due to temperature-to-polarization leakage particularly detrimental. Polarization modulators offer a solution to separate the polarized signal of interest from these unpolarized foregrounds. Many polarization modulation schemes exist Brown et al. 2009, and a rapidly-rotating half-wave plate (HWP) is one of the most promising. The SWIPE polarization modulator unit uses this technique and operates at 1.6 K to reduce the background on the detector produced by the HWP emission Columbro et al. 2019. The technology adopted is based on a superconducting magnetic bearing (SMB) which can significantly reduce the friction. We present the baseline design of the modulator which was already tested on a room temperature mockup (see §3).

The polarization modulator is also one of the key components of the LiteBIRD mission, the next generation satellite mission Hazumi et al. 2020, Lamagna et al. 2020 expected to be operative in $\sim$ 10 years, which will map CMB polarization 20 times deeper than Planck, with a total error of $\delta r < 0.001$, conservatively assuming equal contributions of statistical error, systematic error, and margin. The use of 3 continuously rotating HWPs (for the low, middle and high frequency telescopes) mitigates important systematic errors already observed in Planck data. Their development is more challenging than for SWIPE due to the spacecraft requirements and the Technology Readiness Level (TRL) required. The possibility to use a scaled design is discussed in §3.7.

2. Multi-mode receivers

The SWIPE instrument uses multi-mode receivers, a choice which boosts the sensitivity of the instrument, at the expense of angular resolution (which is not required for a large-scale polarization survey), simplifying the readout

and data processing. In the focal plane, 20 mm aperture horns are coupled to large detector absorbers (10 mm mm diameter, see Fig. 1), with the TES sensor located on the side of the spider-web absorber. The pixel assembly has been checked at room temperature and tested at the bolometer base temperature of 300 mK, inside a custom cryogenic testbed, looking at a Gunn oscillator (128 GHz) located in the far field. We developed a custom cryogenic neoprene absorber, in addition to the stack of standard metal meshes low-pass filters. Such development reduced the background on the detector at a level similar to the one expected in flight, allowing to measure the main beam of the pixel assembly. The measured FWHM is 21°, slightly narrower than the one (24°) required for optimal coupling to the telescope lens, due to vignetting produced by the filters stack.

2.1. Horn and detector design

The key design guideline of SWIPE is to focus on the efficient collection of microwave photons and on the polarization purity Legg et al. 2016. In order to optimize the collecting efficiency, we rely on a multi-moded coupling of the radiation to the detector. We assume that each of the modes transports the same fraction of the available radiative power from free space to the absorbing element of the detector, and that the contributions from the modes add incoherently to determine the total power collected by the system. Under these assumptions, a multi-mode system at frequency ν has a theoretical throughput, $A\Omega(\nu) = N_m(\nu)\lambda^2$, where A is the effective collection area, Ω is the effective solid angle of acceptance of the system, λ is the free-space wavelength of the photons and N_m the number of modes collected. The signal-to-noise ratio of an individual detector scales as

$$SNR = \frac{\int B(\nu)\epsilon_{BP}(\nu)A\Omega(\nu)d\nu}{\sigma_{PNL}} \propto \langle N_m(\nu)\rangle^{1/2}, \quad (1)$$

where $B(\nu)A\Omega(\nu)d\nu$ is the power collected from a source of brightness B within a band $d\nu$ centered at frequency ν, ϵ_{BP} is the frequency-dependent bandpass efficiency, σ_{PNL} is the signal variance, and the brackets in the last term highlight a weighted average over the instrument passband. Therefore, an instrument with multi-moded coupling exhibits the same sensitivity per detector as N_m individual single-moded sensors, sacrificing high resolution which is not required for B-mode polarization detection Hiramatsu et al. 2018. The obtained FWHM is 1.4°.

$\nu_{\rm eff}$ (GHz)	145	210	240
HPBW	30%	20%	10%
$N_{\rm m}(\nu_{\rm eff})$	13	26	34
$N_{\rm m}(\nu_{\rm low})$	10	23	32
$N_{\rm m}(\nu_{\rm high})$	17	32	39
$A\Omega$ (cm^2 sr)	0.56	0.53	0.53

Table 1. Basic parameters of the SWIPE pixels, including effective frequency, half-power bandwidth (HPBW), number of modes selected at the nominal frequency by the waveguide selector in the horn-cavity assembly, variation in the mode coupling at both edges of the band, and nominal system throughput.

The mode selection in the SWIPE pixels is performed by feeding radiation from a smooth conical horn into a cylindrical waveguide acting as a mode filter. A basic treatment of the cylindrical waveguide modes allows to tune the guide diameter in order to get the desired number of modes per channel. The SWIPE pixel assemblies employ 4.5 mm diameter, 10 mm long waveguides connecting the output of the horns to the tapered transition, which feeds a cylindrical cavity hosting the multi-mode absorber. With the chosen waveguide, the SWIPE detectors couple to different numbers of modes, as listed in Tab. 1. The characteristics of the antenna are shown in Fig. 1.

The cross-section of the multi-moded simulated beam pattern at 145 GHz (the frequency used during tests) is shown in Fig. 2. The FWHM is 24° and the working half aperture defined by the stop located just before the HWP is 30°.

The detector absorber Biasotti et al. 2014 is a large (10 mm diameter) Si_3N_4 membrane

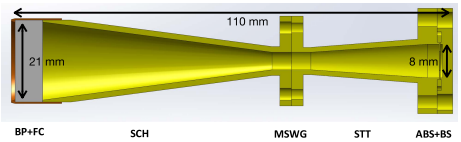

Fig. 1. Schematic of the SWIPE pixel assembly, highlighting the bandpass filter and filter cap (BP+FC), the smooth conical horn antenna (SCH), the mode-selecting waveguide (MSWG) and the smooth tapered transition (STT) hosting the multi-mode spider-web absorber and its backshort (ABS+BS).

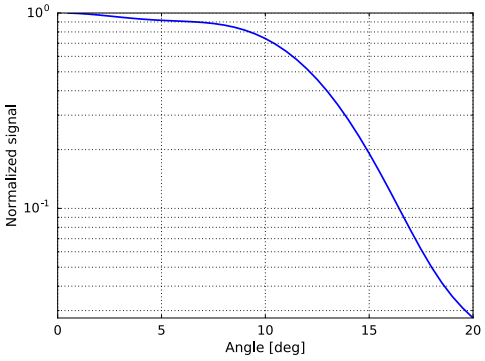

Fig. 2. Beam cross section at 145 GHz.

with a mesh size of 250 µm, suspended with a thin legs structure (Fig. 3) and designed to minimize its cross section for incident cosmic rays, which are potentially very dangerous for CMB measurements in the stratosphere Masi et al. 2010. The transition-edge sensor (TES) is a Ti/Au bilayer with $T_c \sim 550$ mK (detail of Fig. 3), thermally coupled to a Bi/Au microwave absorber.

Near the transition temperature T_c, TES detectors exploit the sharp resistance variation of a thermistor which enables to measure extremely small temperature variations occurring in an absorber upon absorption of a photon. The bolometer was designed to work in the stratospheric background, so $P_{tot} = P_{bias} + P_{opt} < P_{sat}$ where P_{bias} is the power used to bias the bolometer, P_{opt} the optical power which comes from the sky and P_{sat} is the saturation power (~ 25 pW in the case of samples under testing).

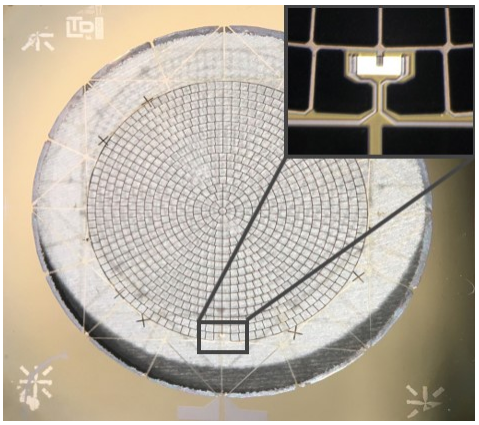

Fig. 3. Detector absorber membrane (10 mm diameter). The TES detector is located in the bottom part of the external ring.

Testing the detectors at the cryogenic base temperature is very challenging because of multiple difficulties: the detector should be cooled down up to 300 mK; the background on the absorber should be reduced below the detector saturation power by means of a filter chain; the magnitude of standing waves introduced by the filters should be minimized as much as possible to neglect its impact in the beam pattern.

We use a three-stage dry cryostat (Fig. 4) composed of a pulse tube mechanical cryocooler[1] whose cold head cools down the first two stages to about 40 K and 4 K and a ^{4}He/^{3}He fridge to cool down the last stage to about 300 mK.

A 120 mm diameter, 6 mm thickness high-density-polyethylene (HDPE) window is located on the bottom of the external shell. A thermal shader is mounted on internal side of the window to reject the far infrared radiation. We developed a new absorber made of neoprene which was coupled with a set of filters (10 cm^{-1} low-pass filter, 12 cm^{-1} low-pass and FluoroGold on the 4 K stage and 15 cm^{-1} low-pass filter on the 40 K stage) to reduce the background on the detector. Without this kind

[1] Sumitomo Heavy Industries Ltd

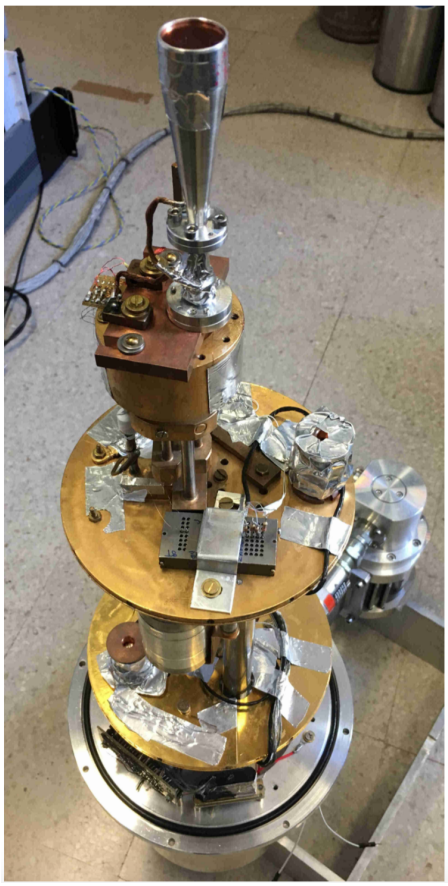

Fig. 4. Picture of the cryostat inner stages (upside down). The antenna is mounted on a copper plate on the evaporator while on the second stage is visible the SQUID series array box.

of absorber, the most common technique consists in using a configuration with two reflective neutral density filters (NDF, transmission $\sim$ 1% each) mounted at room and/or cryogenic temperature. Due to the high reflectivity of NDFs which reflect back most of the radiation, using 2 parallel NDFs produces standing waves which can impact significantly on the beam pattern measurements. The simplest way to solve this issue consists in tilting the filters, one with respect to each other, with a tilt across the filter surface larger than the test wavelength. However, in our configuration, tilting the filters increases the distance between the horn and the window, reducing the free aperture of the system and the beam tails are strongly affected by diffraction produced by the rings of the tilted filters stack. This is the main reason why we decided to develop this innovative technique based on a neoprene absorber which allows to cooldown the detector up to 300 mK with a $P_{opt} \lesssim 15$ pW.

The beam pattern measurements Columbro et al. 2020 are performed by means of a tunable D-band Gunn oscillator, movable on graduated rails in an x-y plane located in the far field of the pixel assembly antenna under test (while the z axis is the optical symmetry axis of the antenna). The linear coordinates x, y were then converted to angular coordinates. The Gunn oscillator ($\sim$ 10 mW in the range 115 GHz-145 GHz) feeds a rectangular antenna (25 dB gain[2]) through a variable attenuator, and is modulated according to an input reference coming from a function generator.

Fig. 5 shows the simulated and the measured 2D beam maps ($AR_{Tot}(\theta_x, \theta_y)$) which are the combination of the Gunn angular response ($AR_G(\theta_x, \theta_y)$) and the antenna angular response ($AR_{Ant}(\theta_x, \theta_y)$):

$$AR_{Tot}(\theta_x, \theta_y) = AR_G(\theta_x, \theta_y) \cdot AR_{Ant}(\theta_x, \theta_y). \quad (2)$$

When compared to the NDFs configuration beams, the measured beams do not present bumps or lacks of radiation and their shape is close to the expected one but is not in full agreement: by using Eq. 2 the measured antenna FWHM is 21° for the p-polarization beam, while the expected one is 24° (Fig. 5). The width of the main peak is similar but there are some features in the measured beam which are not expected. This discrepancy could be due to vignetting induced by the cryostat window and filters stack (geometrically seen as a ±12° stop). The issue will be solved by the measurements in the LHe SWIPE cryostat, where the 500 mm diameter aperture allows for pixel beam patterns without vignetting.

[2] `http://www.aerowave.net/Catalog/28.pdf`

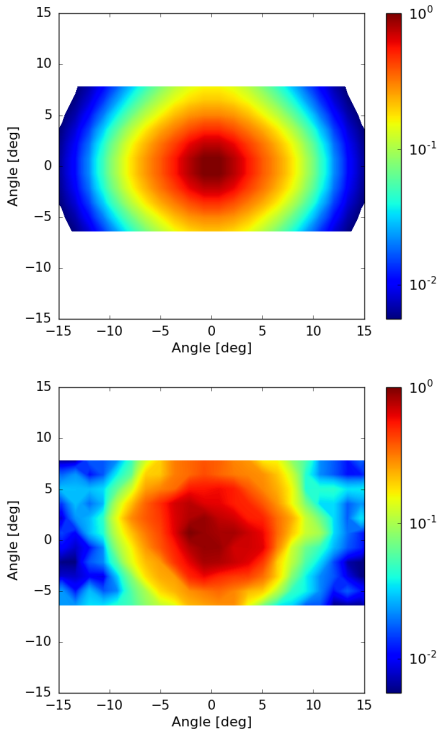

Fig. 5. Measured beam (b) compared to the simulated beam (b) combined with the Gunn antenna response. Each beam is normalized to its maximum.

3. LSPE/SWIPE polarization modulator

The LSPE/SWIPE polarization modulator unit is composed of a continuously rotating HWP (500 mm), cooled down at ∼1.6 K with a power dissipation much smaller than the other heat loads on the superfluid helium bath of the instrument. The main requirements of the modulator are summarized in Tab. 2.

The rotator is based on a superconducting magnetic bearing (SMB) Klein et al. 2011, Hill et al. 2018, Sakurai et al. 2018, a solution which uses a high-temperature superconducting (HTS) magnetic bearing to hold a rotating HWP. Typically this support consists of a ring-shaped permanent magnet (PM) magnetized in the axial direction and an array of HTS tiles. In the SWIPE polarimeter we plan to use a SMB to rotate a large (500 mm) cryogenic (1.6 K) metal-mesh HWP. The modulator is conceptually similar to the EBEX one EBEX Collaboration 2018, Johnson et al. 2017, but more challenging and ambitious because the size of the HWP (500 mm diameter) will make the SWIPE modulator the largest ever tested. At variance with the most common design of a superconducting magnetic bearing Hill et al. 2018, we choose a different SMB configuration (Fig. 6): the magnet ring and the superconductor are not stacked up but the internal rotating ring is the magnetic one and the external is the superconductor one, in order to obtain a side face to face interaction and avoid any possible horizontal displacement

Parameter	Requirement
HWP diameter	500 mm
Mechanical frequency	0.5 Hz
Encoding accuracy	0.1′
Power budget	< 35 mW
Base temperature	1.6 K
Total mass	< 25 kg

Table 2. Requirements of SWIPE polarization modulator.

The selected superconductor (YBCO) is the type-II superconductor with the highest pinning force and critical current density (∼ 10^5 A mm^{-2}). Higher critical current means lower hysteresis losses Bean 1964. Due to the high cost of large volume superconductors we decided to use a segmented ring of 18 YBCO tiles. The rotor (Fig. 6) is composed of 3 stacked rings, starting from the bottom:

- Groove ring: used to clamp the plate at room temperature or before the reheating.
- Magnetic ring: composed of 2 Neodymium magnetic rings and 3 thin iron rings to produce a more uniform magnetic field.
- Aluminum ring with three different functions: hold the HWP in the center, measure the angular position of the rotor with the encoder and hold the small magnets used as the motor.

Three clamp and release systems evenly spaced on the external diameter are cou-

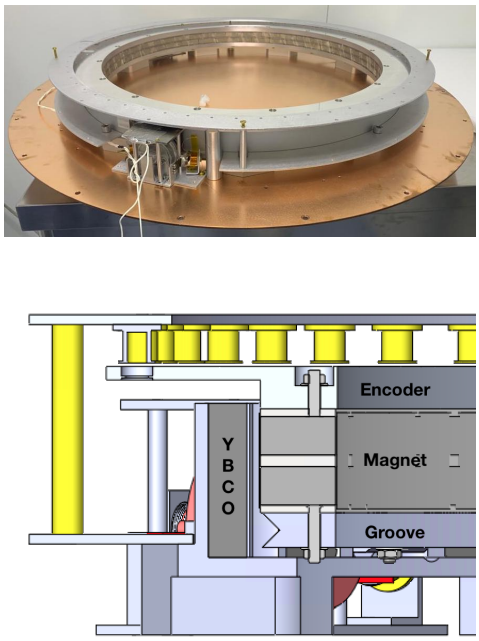

Fig. 6. (*Top*) PMU during the installation in the cryo facility. (*Bottom*) PMU section: the inner ring is the rotor while the outer is the stator; on the top of the rotor there is the coils ring (yellow).

pled with the groove ring and keep in position the rotor when the temperature is greater than the superconductor critical temperature. The clamp/release system Columbro et al. 2018 has: large rotor mass compliance ($\sim$ 10 kg); zero power dissipation while holding the rotor, zero power dissipation when the rotor is released; fast ($\sim$ 40 ms), balanced release and clamp actions, low power dissipation ($\sim$ 30 J) on the cold stage during each operation; low cost; and high reliability over hundreds operation cycles. We expect to clamp and release the rotor only once at the beginning of the flight, nevertheless the system was designed to be able to clamp and release the rotor as many times as necessary.

The PMU is also equipped with a custom capacitive sensors to measure the temperature and levitation height of the rotor de Bernardis et al. 2020. The temperature sensor is a thermistor, physically mounted on the rotating device and biased with an AC current, which is transferred from the steady electronics to the rotating device via capacitive coupling. The levitation height sensor is a network of capacitors, similar to the one used for the capacitive coupling of the thermistor. The system reaches an accuracy better than 3% for the measurement of the thermistor resistance, and an accuracy of $\sim$ 10 μm for the measurement of its levitation height. Any tilt of the rotor might introduce systematic effects in high precision applications D'Alessandro et al. 2019 and could be dynamically sampled by replicating the readout chain and the assembly of static poles in three replicas separated by 120° in azimuth.

3.1. Motor design

The rotation is induced by an electromagnetic motor based on the interaction between 8 small magnets placed on the rotor coupled with 64 driving coils mounted on the stator. By modulating the current in each coil we are able to simultaneously push/pull the nearest magnet.

The choice of the magnets material is critical because of a possible modification of the demagnetization characteristics at cryogenic temperatures. The NdFeB undergoes a spin reorientation as the temperature falls. Most reports García et al. 2000 find a spin reorientation at 135 K due to an unusual combination of anisotropy constants and other factors. This demagnetization causes also a decrease of the magnetic field of about 20%. A possible solution to avoid both problems is to use Samarium Cobalt magnets ($SmCo_5$ or Sm_2Co_{17}) which are used without any issue below 2 K Trout and Graham 1976.

In the rotor of SWIPE we use 8 SmCo magnets evenly spaced at 45°, with 8 mm diameter and 2 mm thickness. The residual flux density is $B_{r_{max}} \approx 1.1$ T giving a magnetic dipole moment $m \approx 0.9\,\mathrm{A\,m^2}$.

In order to chose the best design to minimize friction produced by the small drive magnets, we simulate the eddy currents produced by their AC magnetic field variation using the COMSOL Multiphysics software. The ex-

pected magnitude of power loss induced by eddy current loss is 2.6 mW, compatible with what we measured Columbro et al. 2021.

These magnets are coupled with the magnetic field produced by the solenoids. The axial magnetic field produced by an ideal solenoid is $B = Ni\mu$, where μ is the magnetic permeability, N is the number of turns and i is the current. Given an arbitrary value of the magnetic field, if we want to use the smallest possible current, we can both increase the number of turns (or modify the geometry of the coil) or increase the magnetic permeability. In case of air core coil, the magnetic permeability is $\mu = \mu_0$ while with a ferromagnetic core, the permeability increases by a factor μ_r. Because of the modulated current and the proximity of moving magnets, the ferromagnets should be magnetized and demagnetized. At low temperature the hysteresis loop is enlarged and so the ferromagnet could dissipate too much power or remain magnetized. For this reason we decided to use air coils with optimized geometry to increase the force and low resistance to minimize the Joule losses. The coils geometry chosen corresponds to 8 mm length and 7.8 mm diameter with 240 turns of 0.2 mm diameter copper wire (residual resistivity ratio equal to 30).

3.2. Drive system

We developed a custom electronics (top panel of Fig. 7) to control the spin of the rotor. All electrical components are qualified for the stratospheric pressure (∼ mbar) and certified up to -55°. The electronic box will be heat sinked to a heater at a temperature > −40° to remain warmer than the external environment (∼ −70°). The central idea of the drive system is a PI (Proportional-Integrated) feedback control composed of two optical encoders, an electronic platform, a voltage generator and the coils. A schematic diagram is shown in Fig. 8. The PI feedback controls both the frequency of pulses (allowing to spin up the rotor) and the magnitude of the current 8 times per round, to stabilize the rotation when the right frequency is reached. We decide to not use the classical PID controller with the derivative term because we do not expect fast variations of the rotational speed due to the high inertia of the system.

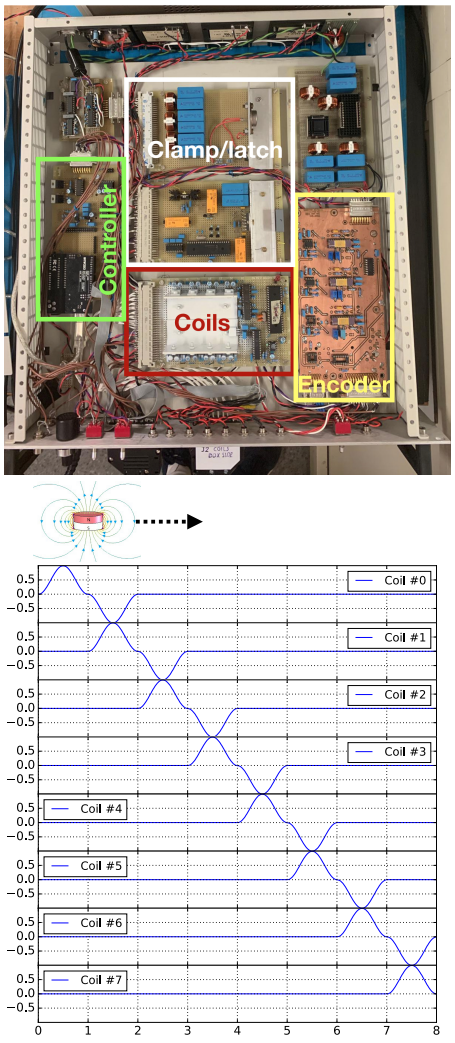

Fig. 7. (*Top*) Electronics control box, composed mainly of 4 different boards: the microcontroller, the voltage generator, the clamp and latch controller and the encoder readout. (*Bottom*) Smooth current pulses generated to supply the driver coils and push/pull on the rotor magnets.

The electronic platform chosen is Arduino. The initial parameter given by the user at the beginning is the target frequency of the rotor

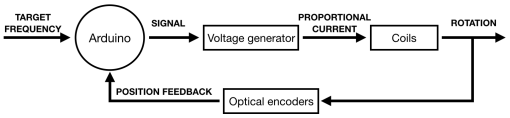

Fig. 8. The PI feedback control: the user choses the target frequency, Arduino gives a signal to a current generator to control the amplitude and the frequency of the current in the coils. Two optical encoders monitor the position and the speed of the plate.

which should be changed during the operation. Knowing the position of the 8 magnets (one every 8 slits), the relative phase of current in each series of coils is determined (bottom panel of Fig. 7). The maximum value of the current is reached when the magnets are in the middle of two coils. There is another small phase dependent on the frequency, added to optimize the system.

In the first version of the electronics we made a voltage generator with output voltage of 6.35 V_{PP} allowing a maximum average current of ~ 55 mA (~ 1 A at 1.6 K). On the other hand, we measured a back electromotive force produced by the small magnets of 4 $V_{PP}Hz^{-1}$, so the effective current flowing in the coils is:

$$\bar{i}[A] \simeq \frac{0.25}{R[\Omega]}(V_{PP}[V] - 4f[Hz]) \quad (3)$$

For this reason we decided to switch to current generators, with the same voltage amplitude and high impedance ($\sim$ kΩ).

3.3. Coil design optimization

By assuming the same radius $R = 296$ mm for all drag forces, we can find a coarse estimate for the required force for a spin rate of 1 Hz:

$$F_{drag} = \frac{P}{v} = \frac{P}{2\pi f R_*} \simeq 5 \times 10^{-3}\,\mathrm{N} = 8\,\mathrm{mN} \quad (4)$$

where the assumed total power dissipated by the rotor is 15 mW.

The strongest force is required when a magnet is in the middle between two coils which is also the point where the force profile is minimum. In this configuration we can assume the magnet as a magnetic dipole $\boldsymbol{m} = m\hat{z}$ where the magnetic dipole moment is related to the volume V and the residual flux density B_r of the magnet by

$$m = \frac{B_r V}{\mu_0}. \quad (5)$$

With this assumption, the force produced by one coil acting on the magnet is:

$$\boldsymbol{F} = \boldsymbol{\nabla}(\boldsymbol{m} \cdot \boldsymbol{B}) = m\boldsymbol{\nabla}B_z. \quad (6)$$

The radial component is the one which induces the rotation of the bearing rotor. Fig. 9 shows the force magnitude as a function of the magnet position between two nearest coils. The mean force per unit current given on a single magnet is 35 mN A^{-1} which corresponds to a total force (8 magnets) of 280 mN A^{-1} and requires an average current $\sim$30 mA (thanks to Eq. 4).

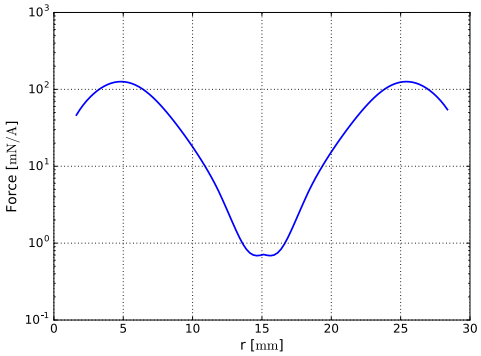

Fig. 9. Force magnitude as a function of the magnet position between two nearest coils.

The coils were divided in 8 series with total resistance as homogeneous as possible ($\sim$27.6 Ω). After the assembly on the support ring the final resistance of each series becomes 28.6$\pm$0.1 Ω. The increased resistance is due to connections between coils and the connector on the stage. In addition we add a series of 8 coils used to start the rotation if the motor magnets are located exactly between two motor coils (Fig. 10).

The expected resistance in the cryogenic environment is $\frac{28.6\,\Omega}{RRR} = 1.0\,\Omega$. The circuit can

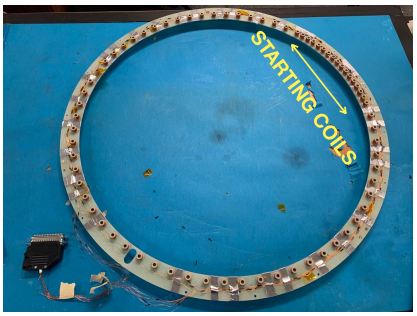

Fig. 10. Motor coils installed on a G10 ring. The additional starting coils are located on the opposite side of the encoder (the hole in the G10 ring).

be sketched as an RL series and the current in each coils is:

$$i = \frac{V_{in}}{R + j\omega L} \tag{7}$$

where V_{in} is the input voltage, $R \sim 9.5{+}1.0\,\Omega$ the resistance of the wires between room and cryogenic temperature and the resistance of one coil series ($1\,\Omega$, see §3.6) and $L = 1.9$ mH the inductance of the series. Because the condition $R \gg \omega L$ is verified we expect a constant value of current for applied input voltage at different frequencies during the acceleration phase.

3.4. Encoder readout system

The readout position system for the PMU is based on an optical encoder, based on light shining onto a photodiode through slits in the rotor. There are two different encoders: an absolute one with a single slit and a relative one composed of 64 evenly spaced slits (3 mm diameter). To avoid possible dissipation of LED or photodiode at cryogenic temperature, we use two pairs of optical fibers. Each pair consists in a fiber connected to a transmitter (HFBR-1412TMZ[3]) at room temperature, reaching the top surface of the encoder chopper ring, and a return fiber starting from the bottom surface of the optical chopper and reaching the detector (BPX61 photodiode[4]) at room temperature.

The transmitted signal is modulated at a frequency of 31 kHz produced by a quartz crystal oscillator circuit. The signal detected by the photodiodes is pre-amplified and then demodulated and amplified again by an AD630 lock-in, allowing to separate a small narrow-band signal from large amounts of uncorrelated noise produced by the significant light loss due to an air-gap of about ∼10 mm between the back-to-back optical fibers. The fibers are mounted in a PEEK holder to eliminate eddy currents due to the proximity to moving magnets. The signals produce high/low pulses which are transmitted to a single-board microcontroller. When the level of signal is above a threshold, a timestamp is settled with a µs resolution, giving an angular resolution better than 0.01°. The conductive heat load produced by the 4 optical fibers is $\lesssim 50\,\mu$W.

Due to the high inertia of the system, all measurements of the position are correlated. We introduce a Kalman filter which uses the dynamic model and the physical properties of the system, and multiple sequential measurements to make an estimate of the varying quantities that is better than the estimate obtained by using only one measurement alone. The input parameter of the filter are the error on the readout data retrieved with the previous estimation and the uncertainty on the acceleration of the system estimated using the rotor inertia and the variation of the coils torque. The results of the Kalman filter application are shown in Fig. 11 and are compared with the accuracy corresponding to the electronic readout resolution (1 µs). The current configuration is not limited by the electronic readout resolution but only by the stability of the rotation. This stability is limited by the current generator resolution which uses a 12-bit DAC. An improvement (from 12-bit to 16-bit) of the resolution is already planned but is not required for the SWIPE/LSPE modulator which has a requirement of $\sigma_{\omega_{HWP}}/\omega_{HWP} = 5 \times 10^{-6}$ at 0.5 Hz.

[3] https://it.rs-online.com/web/p/trasmettitori-a-fibre-ottiche/8019229/

[4] https://it.rs-online.com/web/p/fotodiodi/6547785/

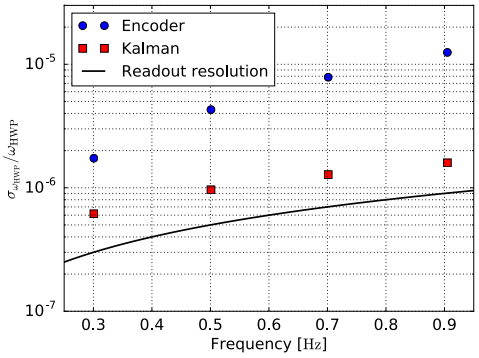

Fig. 11. The raw accuracy of the encoder data (blue dots), the accuracy resulting from the use of a Kalman filter (red squares) and the accuracy corresponding to the electronic readout resolution (1 µs).

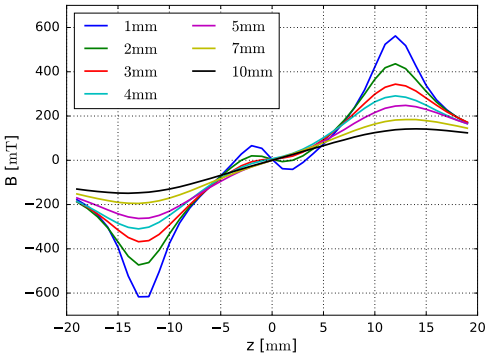

Fig. 12. Magnetic field as a function of height ($z = 0$ mm is the center of the middle iron ring) for various distances from the main magnet.

3.5. Eddy current loss

Every inhomogeneity of the magnetic field induces loops of electrical current in the conductive materials. They can be generated by a time varying magnetic field ΔB and dissipated as Joule heat. The power loss due to eddy currents per unit volume is:

$$P \propto \sigma(\Delta B)^2 d^2 f^2 \tag{8}$$

where σ and d are the conductivity and the thickness of the material. Eq. 8 represents a rough estimate of the power loss without considering the skin effect and derived using other approximations. Nevertheless the strong dependence on frequency, on the magnetic field inhomogeneities and on conductivity is clear. The main contribution comes from the HTS tiles holder because its distance from the magnet is a few millimeters, so the best solution could be the use of a dielectric material, like fiberglass, vespel or PEEK ($\sigma \sim 0\,\mathrm{S\,m^{-1}}$). On the other hand, thermalizing HTS tiles surrounded by these materials with a very low thermal conductivity coefficient could become a problem. At room temperature the best candidates are copper and aluminum ($\rho_{Cu} = 17.2\,\Omega\,\mathrm{nm}$ and $\rho_{Al} = 26.5\,\Omega\,\mathrm{nm}$), but at 4 K the best compromise is an aluminum support as the resistance ratio is $\frac{\rho(300\,\mathrm{K})}{\rho(4\,\mathrm{K})} \sim 2-3$ for aluminum and $\frac{\rho(300\,\mathrm{K})}{\rho(4\,\mathrm{K})} \sim 10-50$ for copper[5]. Despite the heat transfer of copper is twice as much as aluminum, the second has a lower electrical conductivity. The second important parameter is the magnetic field inhomogeneity. A more homogeneous main magnet ($\frac{\Delta B}{B} < 5\%$) helps to reduce drastically this contribution.

The main magnet was designed to maximize the magnetic field in proximity of the superconductors and minimize inhomogeneities. It is made of 2 neodymium rings sandwiched between three iron rings. Each neodymium ring is splitted in 32 segments and the junctions are out of phase to reduce the inhomogeneities.

The magnetic field is monitored by means of a Hall sensor[6] also suitable for cryogenic application. The power dissipation in the sensor is 180 µW with a bias current of 10 mA over a 1.8 Ω resistance. Measurements (Fig. 12) are performed at different heights and distances from the steady magnet. Both peaks coincide with the upper and lower iron rings while the center (~ 0 mT) coincides with the middle.

For the measurement of dissipation power, the main magnet is installed on the room temperature rotor and spins while the Hall sensor monitors the magnetic field for different

[5] https://trc.nist.gov/cryogenics/materials/materialproperties.htm

[6] https://www.cryomagnetics.com/products/hall-effect-sensors/

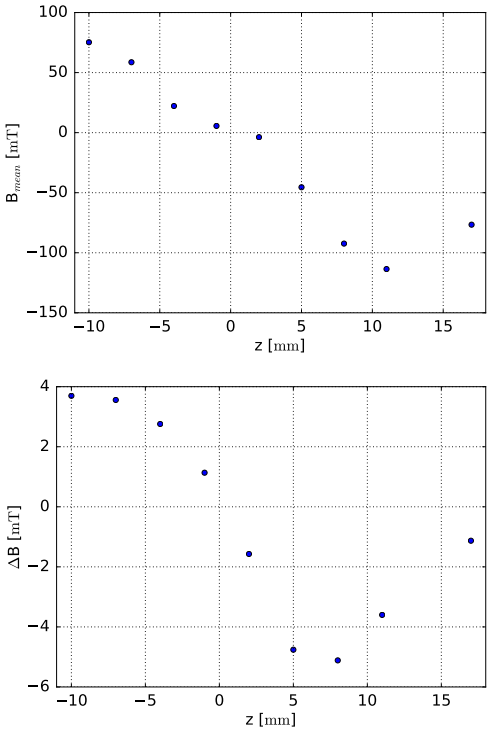

Fig. 13. Magnetic field average (*top*) for different quotes at few mm from the magnet and the relative inhomogeneities (*bottom*).

heights at a fixed distance of a few mm. After a removal of sine component induced by a slight misalignment of the rotation axis ($\sim$ 0.5°), Fig. 13 shows the magnetic field average for each quote and the relative inhomogeneity. At the peak of the magnetic field, the relative inhomogeneity corresponds to $\lesssim 3\%$.

We removed all conductive materials around the YBCO holder, in this way the only contributions to friction comes from the eddy currents on the YBCO holder produced by the main magnet. The friction produced by the main magnet at 1 Hz is 6.2 mW.

Other sources of eddy currents are the small magnets used in the motor. A dipole of moment m, oriented vertically, which is moving at height z_0 above a conductive plate produces a power loss Reitz 1970:

$$P = Fv = \frac{3\mu_0 m^2}{32\pi z_0^4} w \left[1 - \frac{1}{\sqrt{1 + \left(\frac{v}{w}\right)^2}}\right] \quad (9)$$

where v is the magnet velocity and $w = \frac{2}{\mu_0 \sigma \delta}$ related to the conductivity of the plate and to its thickness δ. The estimated friction induced by the motor magnets is 0.8 mW (see Columbro et al. 2021 for further details about the test).

3.6. Harness

An important factor to achieve low base temperature is making sure that the power load on the colder stage is minimized. All the electrical wires required to drive the rotation and read its status also conduct heat from the warmer stage to the colder one.

The formula for heat flow is:

$$Q = \int_{T_1}^{T_2} \frac{A}{L} k(T) dt \quad (10)$$

where Q is the heat flow, $k(T)$ is the thermal conductivity of the material, A and L are the cross-sectional area and the length of the wire and T_1 and T_2 the temperatures gradient across the wire. The cross sectional area and the length of the wire can greatly affect the heat loss: too short of a wire will cause heating, too long of a wire will increase its resistance which may impact the circuit function and increase the power dissipated in the wire itself.

The choice of the wire material depends on the thermal conductivity and in particular on its dependence on temperature Powell et al. 1966, Tuttle et al. 2010. While the best choice for the thermal conductivity point of view is the manganin wire, the resistance is very high and can considerably increase the Joule loss:

$$P_J = Ri^2 \quad (11)$$

where R is the resistance and i the current.

In practice, for our polarization modulator unit we have a bundle of 16 cables for the motor: 8 carrying the driver coils currents (8

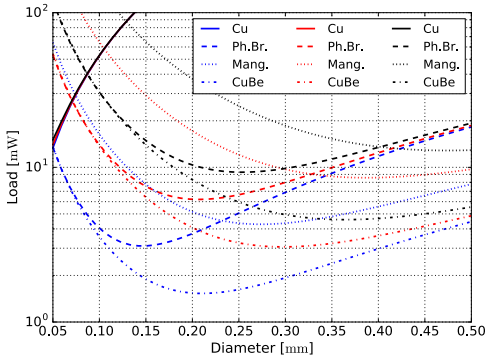

Fig. 14. Heat load produced on the 1.6 K stage for different wire materials and different current values (20 mA in blue, 40 mA in red and 60 mA in black). In the most likely case (40 mA), the manganin (dotted lines) produces $\sim$ 10 mW heat load while the behaviour of phosphor bronze (dashed lines) and Beryllium-Copper (dash-dotted lines) is very similar for lower wire diameters.

phases) and 8 for the return currents. We reduce electromagnetic interference by twisting the drive and return wires separately for each phase. The total heat load on the cold stage is the sum of the conduction loads and the power dissipation loads for all these wires. Fig. 14 shows the power load on the coldest stage (1.6 K) for different materials and currents as a function of the wire diameter. The Beryllium-Copper wire minimizes the heat load and the diameter chosen is 0.25 mm with 0.05 mm of Heavy Polyimide (HML) insulation[7].

The resulting heat load is 5-7 mW on the 180 K stage, 5-8 mW on the 65 K stage and $\sim$ 3 mW on the 1.6 K stage. The total resistance for a single wire is 4.7 Ω (3 m length).

3.7. Expected performance

The performance measured for the LSPE/SWIPE modulator at 300 K and the performance we expect at 1.6 K (given the room temperature measurements), are summarized in Tab. 3 for a rotation frequency of 0.5 Hz. Material properties, such as electrical conductivity, thermal conductivity and YBCO critical current, were assumed to be the same as 4 K Habisreuther et al. 2000.

	300 K	1.6 K
8 magnets	0.8	2.2
Main magnet	1.3	3.5
Hysteresis	-	10
Joule	645	6.1
Harness	-	3.2
Bearing	41.5	-
Total	690	25

Table 3. Heat load in mW measured at 300 K and expected at 1.6 K for a rotation frequency of 0.5 Hz.

In the first configuration the friction produced by the motor magnets is 9.2 mW. Most of this power comes from eddy currents produced on the aluminum ring which holds the coils in place. By replacing this ring with a G10 once the residual contribution is 0.8 mW. By assuming a RRR = 2.8 of aluminum (6082-T6) the expected contribution at cryogenic temperature is 2.2 mW.

As for the friction produced by the main magnet inhomogeneities, we measure 1.3 mW, meaning an expected value of 3.5 mW which should be reduced even more by the presence of the superconductor which will shield part of the magnetic field.

The hysteresis contribution will be tested only in the cryogenic environment. Since the mass of the rotor is 9.5 kg and the vertical spring constant of the system is 2-3×10^5 N m^{-1}, we expect a fall of the rotor after the release < 0.5 mm. Starting from Davis et al. 1988 and from the magnetic field profile we can estimate the hysteresis contribution which will be 5-10 mW.

Assuming the worst case the total friction during rotation at 0.5 Hz is 15 mW. Considering the efficiency of the motor, we need $\bar{i} = 45$ mA which produce a Joule heating of 6.1 mW. The total expected power load on the 1.6 K stage is $\sim$ 25 mW which is an acceptable contribution if compared to the total

[7] `https://www.calfinewire.com/index.html`

Parameter	Requirement	
	MFT	**HFT**
Spin rate	39 rpm	61 rpm
HWP diameter	320 mm	220 mm
HWP temperature	< 20 K	
Load on the 5 K stage	< 4 mW	
Angular accuracy	$< 1'$	$< 5'$
Total mass	< 20 kg	

Table 4. MHFT-PMU main requirements.

$\sim$ 180 mW present on the superfluid helium bath of LSPE/SWIPE and does not considerably impact the duration of the flight ($\sim$ 15 d).

The middle and the high frequency telescope of LiteBIRD will use the same technology and a scaled design of the modulator described before as the baseline Columbro et al. 2021. On the other hand there are a lot of more stringent requirements in terms of mass, dimension, stiffness, power dissipation, and TRL, for the levitation, driving and gripping mechanisms as well as position encoder. The most important for both PMUs are summarized in Tab. 4.

The most stringent one is the power load on the 5 K stage. In order to meet this requirement and the other ones, a further optimization of the LSPE/SWIPE design has already been studied but not yet tested experimentally. The concept of the motor is also very similar to the SWIPE one. We plan to use 8 SmCo magnets coupled with 2 rings of 32 coils each, on the top and on the bottom of the rotor to obtain a larger and more uniform force. The coils are connected in series (4 series of 16 coils each). A reduction of the inhomogeneities of the main magnet magnetic field from $\sim$ 3% to $\sim$ 1% will reduce the eddy currents up to a factor 9. This improvement is complicated but seems feasible because of the smaller dimension of the permanent magnets with respect to the SWIPE one. A further solution for HFT (due to the small radius of HFT magnet $\sim$ 220 mm) consists in the use of a single magnet with only one magnetization which will guarantee more uniformity.

The main contribution of motor eddy currents comes from the YBCO holder. Making the holder of electrical insulator like G10 will cancel eddy currents but will thermally insulate the superconductor ring. This solution becomes critical in terms of the superconductor cooling. The possibility of using an electrical insulator for the upper part of the holder and a thermal conductor (aluminum) for the lower part is under study.

We also expect hysteresis losses to be very small. This is due both to the effective absence of gravity which keeps in position the rotor after the release and to the low inhomogeneities of the magnetic field which minimizes hysteresis in the superconductor. We estimate a contribution $\ll$ 0.5 mW which will be neglected in our estimation but have to be measured during tests.

The decrease of the total friction will reduce the required current by a factor $\sim$ 10 and the increasing of the RRR from 30 to 100 will make Joule losses negligible.

A first analysis gives a total heat load compatible with the requirement ($<$ 4 mW). Further details are reported in Columbro et al. 2021.

4. Conclusions

The performance of key subsystems like the receivers and the polarization modulator will give to the future experiments the capability to detect the polarization of the CMB at large angular scale, in particular to constrain the B-modes produced by tensor perturbations. The multi-mode receivers and the polarization modulator unit of LSPE/SWIPE were presented. The multi-mode pixel assembly was cryogenically tested at 300 mK. The background on the detector was reduced at a level similar to the in-flight one thanks to a custom cold neoprene absorber. The tests demonstrate that the assembly does not introduce any sharp feature or bump in the beam and its FWHM is a little bit narrower ($\sim$ 10%) than the simulated one but wider than the single-mode one.

The design of the SWIPE polarization modulator was described from different aspects: general design, motor and driver design,

accuracy, losses and harness. Each subsystem was already tested by means of a room temperature mockup, highlighting that the most critical aspect is related to the inhomogeneities of the main magnet magnetic field. The expected heat load during operation is < 25 mW, less than 15% of the total heat load on the superfluid He reservoir.

We also discussed further improvement of this system which will be implemented for the polarization modulator units of the middle and high frequency telescopes of the LiteBIRD mission, the next generation spacecraft devoted to CMB measurements.

Acknowledgements. I would like to thank the SAIT award which gives me the opportunity to publish an extract of my PhD thesis. I am grateful to my thesis advisor P. de Bernardis and my referees G. Pisano and T. Matsumura for the useful suggestions. I acknowledge the Sapienza university and the Italian Space Agency which founded this research.

References

Aiola, S. et al. 2012, Proceeding of SPIE, 8446, doi:10.1117/12.926095
Battistelli, E. S. 2020, JLTP, 199, doi: 10.1007/s10909-020-02370-0
Bean, C. P. 1964, Reviews of Modern Physics, 36, doi: 10.1103/RevModPhys.36.31
Benson, B. A. et al. 2014, Proceeding of SPIE, 9153, doi:10.1117/12.2057305
de Bernardis, P. et al. 2012, Proceeding of SPIE, 8452, doi:10.1117/12.926569
de Bernardis, P. et al. 2020, Review of Scientific Instruments, 91, doi:10.1063/5.0005498
Biasotti, M., et al. 2014, JPCS, 507, doi: 10.1088/1742-6596/507/4/042004
Brown, M. L., et al. 2009, MNRAS, 397, doi: 10.1111/j.1365-2966.2009.14975.x
Columbro, F., de Bernardis, P. and Masi, S. 2018, Review of Scientific Instruments, 89, doi:10.1063/1.5035332
Columbro, F. et al. 2019, Astronomische Nachrichten, 340, doi:10.1002/asna.201913566
Columbro, F. et al. 2020, JLTP, 199, doi:10.1007/s10909-020-02396-4
Columbro, F., et al. 2021, Proceedings of the SPIE, 10.1117/12.2577818
D'Alessandro, G. et al. 2019, A&A, 627, doi:10.1051/0004-6361/201834495
Davis, L. C. et al. 1988, Journal of Applied Physics, 64, doi:10.1063/1.341312
EBEX Collaboration, Y., et al. 2018, ApJ, 239, doi:10.3847/1538-4365/aae434
García, L. M., et al. 2000, Phys. Rev. Lett, 85, doi:10.1103/PhysRevLett.85.429
Grayson, J. A. et al. 2016, Millimeter, Submillimeter, and Far-Infrared Detectors and Instrumentation for Astronomy VIII, 9914, doi:10.1117/12.2233894
Gualtieri, R. 2019, JLTP, 193, doi:10.1007/s10909-018-2078-x
Guth, A. H. 1981, Phys. Rev. Lett, 23, doi:10.1103/PhysRevD.23.347
Habisreuther, T. et al. 2000, JOM, 52, doi:10.1007/s11837-000-0143-8
Hazumi, M., et al. 2020, Proceeding of SPIE, 114432F, doi:10.1117/12.2563050
HIll, C. A., et al. 2018, JLTP, 193, doi:10.1007/s10909-018-1980-6
Hiramatsu, T. A., et al. 2018, Phys. Rev. D, 97, doi:10.1103/PhysRevD.97.123511
Johnson, B. R., et al. 2017, Review of Scientific Instruments, 88, doi:10.1063/1.4990884
Klein, J., et al. 2011, Proceedings of the SPIE, 8150, doi:10.1117/12.893669
Lamagna, L., et al. 2020, JLTP, 200, doi:10.1007/s10909-020-02454-x
Lamagna, L., et al. 2020, Proceedings of the SPIE, 1144370, doi:10.1117/12.2579233
Legg, S., et al. 2016, Proceedings of the SPIE, 9914, doi:10.1117/12.2232400
LSPE Collaboration, et al. 2021, JCAP
Masi, S. et al. 2010, A&A, 519, doi:10.1051/0004-6361/201014065
Masi, S. et al. 2019, JCAP, 7, doi:10.1088/1475-7516/2019/07/003
Mennella, A. et al. 2019, Universe, 5, doi:10.3390/universe5020042
Montier, L., et al. 2020, Proceeding of SPIE, 114432F, doi:10.1117/12.2563050
Paiella, A. et al. 2019, Journal of Physics Conference Series, 1182, doi:10.1088/1742-6596/1182/1/012005
Penzias, A. A. and Wilson, R. W. 1965, ApJ, 42, doi:10.1086/148307
Planck Collaboration, et al. 2020, A&A, 641, doi:10.1051/0004-6361/201833887
Polarbear Collaboration, et al. 2020, ApJ, 897, doi:10.3847/1538-4357/ab8f24
Powell, R. W. et al. 1965, National Bureau of Standards, 1
Reitz, J. R.1970, Journal of Applied Physics, 41, doi:10.1063/1.1659166
Sakurai, Y., et al. 2018, IEEE Transactions on Applied Superconductivity, 28, doi:10.1109/TASC.2018.2797302

Thornton, R. J. et al. 2016, ApJ, 227, doi:10.3847/1538-4365/227/2/21
Trout, S. R. and Graham, C. D. 1976, American Institute of Physics Conference Series, 29, doi:10.1063/1.30480
Tuttle, J. et al. 2010, Transactions of the International Cryogenic Materials Conference-ICMC, 1219, doi:10.1063/1.3402333